

ThreshNet: Segmentation Refinement Inspired by Region-Specific Thresholding

Savinay Nagendra¹ Chaopeng Shen² Daniel Kifer¹

¹Department of Computer Science ²Department of Civil and Environmental Engineering
The Pennsylvania State University

University Park

¹sxn265@psu.edu ²cshen@engr.psu.edu ¹dkifer@cse.psu.edu

Abstract

We present ThreshNet, a post-processing method to refine the output of neural networks designed for binary segmentation tasks. ThreshNet uses the confidence map produced by a base network along with global and local patch information to significantly improve the performance of even state-of-the-art methods. Binary segmentation models typically convert confidence maps into predictions by thresholding the confidence scores at 0.5 (or some other fixed number). However, we observe that the best threshold is image-dependent and often even region-specific – different parts of the image benefit from using different thresholds. Thus ThreshNet takes a trained segmentation model and learns to correct its predictions by using a memory-efficient post-processing architecture that incorporates region-specific thresholds as part of the training mechanism. Our experiments show that ThreshNet consistently improves over current the state-of-the-art methods in binary segmentation and saliency detection, typically by 3 to 5% in $mIoU$ and mBA .

1. Introduction

We propose ThreshNet, a post-processing scheme that works with any base neural network that produces confidence maps for binary segmentation tasks (i.e., per-pixel probabilities that indicate the network’s confidence that the true class of a pixel is 1). ThreshNet uses local and global image information to refine the confidence map of the base network and thereby reduce false positives and false negatives in the per-pixel predictions. The effects of this post-processing scheme are illustrated in Fig. 1.

Prior work on binary segmentation [28, 32, 38, 52, 54], based on the pioneering fully convolutional neural network [37], have achieved state-of-the-art results on multiple challenging benchmarks [12, 27, 32, 44]. Despite large improvements in network architectures which employ strate-

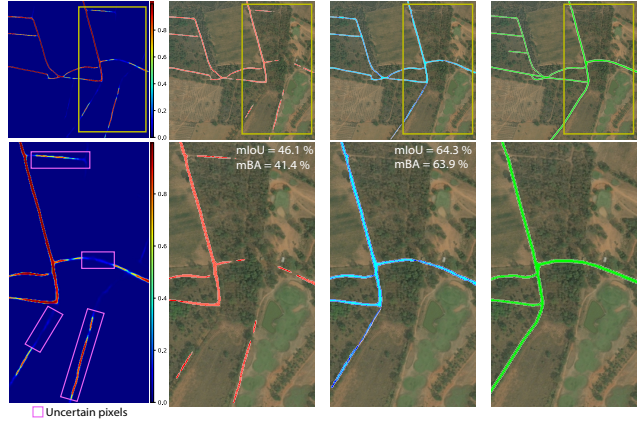


Figure 1. **Performance boost offered by ThreshNet refinement module on a remote sensing image from DeepGlobe [12] test set.** Row 2 has magnified regions marked by yellow rectangles on Row 1. **Column 1:** Predicted probability map from base network D-LinkNet [54] (State-of-the-art). **Column 2:** Thresholded prediction from D-LinkNet [54], with a fixed threshold. **Column 3:** Refined prediction by ThreshNet. **Column 4:** Ground Truth. The corresponding increase in performance after refinement denoted by $mIoU$ and mBA is also shown.

gies such as atrous convolutions [6], skip connections [43], pyramid pooling [20], or densely connected layers [24], they still tend to struggle in boundary areas and other fine structures.

For example, Figure 1 (bottom left panel) shows the confidence map of the state-of-the-art D-LinkNet [54] on a sample image from the DeepGlobe road segmentation dataset [12]. Such a confidence map is normally turned into a prediction by thresholding the pixels at a fixed threshold (which is a standard practice for state-of-the-art methods [28, 30, 52, 54]). This practice would result in both false positives (highlighted by drawn boxes at the top and bottom of the confidence map) and false negatives (in the other two boxes). The average confidence map score of the false

positive regions is ≥ 0.7 and is higher than the average confidence map score of the false negative regions, which is ≤ 0.2 . Thus, no single threshold can eliminate both the false positives and the false negatives – using a fixed threshold results in error-prone predictions such as the second column of Figure 1 and deviate substantially from the ground truth (last column).

In the ideal setting, this problem could be resolved if each image patch had its own threshold. Inspired by this idea, our post-processing method ThreshNet uses patch-specific thresholds during its training in order to learn how they would affect the confidence map. During inference time, a naive idea is to predict what the patch-specific thresholds should be. However, we found that this does not work very well. Instead, ThreshNet tries to predict what the confidence map would look like if the unknown optimal patch-specific thresholds had been used. As a result, we observe improvements in important metrics such as mean Intersection over Union (mIoU) [42] and mean Boundary Accuracy (mBA) [10]. Examples illustrating the types of improvements that result from ThreshNet postprocessing can be seen in Figure 2.

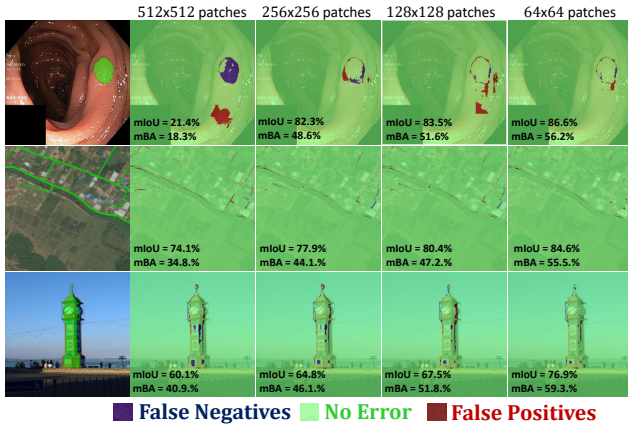


Figure 2. ThreshNet postprocessing and patch size. The images in the first, second and third rows are from the test sets of Kvasir-SEG [27] histopathological dataset, DeepGlobe [12] geospatial dataset and DUTS [44] saliency detection dataset, respectively. **Column 1:** Ground Truth. **Column 2:** Error Map for state-of-the-art methods [28, 52, 54]. **Columns 3, 4 and 5:** Error maps for ThreshNet postprocessing based on patch sizes 256×256 , 128×128 , and 64×64 respectively. The corresponding mIoU and mBA for each error map is also shown. One can observe a significant decrease in false negative pixels (blue) and false positive pixels (red) as patches become more localized.

Our proposed **ThreshNet**, is a memory-efficient, trainable auxiliary network that can be used to improve the confidence map of a trained base network (for example, one can choose a state-of-the-art segmentation network for the base). The confidence/probability map of the base network

is processed through (a) a global branch to capture inter-patch semantics and contextual dependencies and (b) a local branch to capture intra-patch pixel interactions and high-resolution fine structures. ThreshNet is a general scheme that can be appended to any binary segmentation model that generates confidence maps. We evaluate the effectiveness of ThreshNet on geospatial segmentation with the DeepGlobe [12] dataset, and histopathological segmentation with the Kvasir-SEG [27] dataset. We also extend ThreshNet for saliency detection with the DUTS [44] dataset. Our experiments show that ThreshNet consistently improves over the current state-of-the-art methods across these datasets (typically by about 3-5% in mIoU and mBA). Our main contributions can be summarized as:

- We propose ThreshNet, a trainable postprocessing model whose input is a confidence map generated by a base network. Even when the base network is already state-of-the-art, ThreshNet significantly improves mIoU and mBA on benchmark datasets. The key insight is that ThreshNet tries to predict what the effect of optimal per-patch thresholds would be on the input confidence map.
- We show that ThreshNet can also be extended to saliency detection.
- We show that ThreshNet provides inherent boundary refinement, does not require cascading, and achieves competitive accuracy-memory trade-off compared to other refinement schemes.

2. Related Work

Applications using Binary Annotation. Binary annotation is a popular annotation strategy, currently being extensively used in multiple applications [12, 27, 32, 44]. Binary segmentation is used to predict semantic category (foreground or background) for each pixel in an image. Binary segmentation is extensively used in geo-spatial [1, 38, 53, 54] and histopathology [27, 41, 55] segmentation. Saliency detection [18, 23, 44, 52] locates important foreground objects in natural images that could attract human attention.

Segmentation Network Architectures. Previous methods for segmentation [28, 32, 38, 52, 54], based on the pioneering Fully Convolutional Neural Network [37] (FCN) achieved remarkable success on multiple challenging benchmarks [12, 27, 32, 44]. There have been large improvements in extracting contextual information with wide fields-of-view [5, 7, 16, 22] along with FCN’s bottom-up approach for better segmentation quality. This includes feature pyramid methods [11, 20, 36] that spatially pool feature maps of different receptive fields, or dilated convolutions [49]. Encoder-decoder models [2, 8, 31, 34, 35, 39, 43] have also been widely used, where the encoder reduces spatial resolution to capture global semantics followed by a decoder which restores spatial resolution. Skip connections [11, 43]

are further added to recover lost spatial information in deeper layers. Multi-scale context aggregation [4, 7, 19, 47] has proven to be efficient for integrating high-level and low-level features. GLNet [9] uses a three-step training process where a global and a local branch parse downsampled images and image patches respectively, after which a feature aggregation step is used to combine the local and global features. Self-attention [25, 40, 48, 56] has been used in segmentation networks to highlight salient features from spatial-information-rich skip connections and feature maps from deeper layers, where attention coefficients are more sensitive to local regions. Inspired by aforementioned previous network designs, we design ThreshNet to be a residual encoder-decoder architecture with pyramid pooling for context aggregation, skip connections for sharper boundaries, self-attention for highlighting important local regions and multi-scale context aggregation with simultaneously trainable global & local branches.

Segmentation Refinement. Despite large improvements in network architectures which employ the above mentioned strategies, existing methods still show poor boundary adherence and lost of high-resolution fine structures due to uncertainties in predicted probability maps [28, 32, 38, 52, 54]. Researchers have addressed this issue with post-processing refinement strategies. Unsupervised probabilistic frameworks such as CRF [4, 5] or region growing [14, 15] adhere to local semantics without fully leveraging global information. There are methods that exploit only boundary information [50]. Some methods use cascading to aggregate reliable context and structure information [11]. ThreshNet is a trainable refinement module that can effectively and independently leverage both local and global information and also improves upon of refinement modules that use multiple levels of cascading, while requiring much less memory. ThreshNet also provides implicit boundary refinement without an exclusive boundary module.

Adaptive Thresholding. This work should not be confused with *adaptive thresholding* [3], which is a framework for producing black-and-white images based on a threshold that varies with the illumination in different parts of an image.

3. Proposed Method

In this section, we will first build a mathematical model for ThreshNet. We will then describe the overall framework of our auxiliary refinement module, ThreshNet. Finally, we will then discuss the network architecture and loss function.

3.1. Mathematical model for ThreshNet

ThreshNet takes as input, the confidence map produced by a base network. Since the base network has been trained until saturation, we can make an assumption without loss of generality that "it is trying to produce correct (high-

confidence) predictions for most of the pixels." There are however harder-to-segment regions where the base network produces under-confident predictions, which will become false-negative and false-positive regions after thresholding by a fixed (usually 0.5) value. It is these regions that ThreshNet refines to produce results with higher segmentation quality. So, we can assume that the distribution of confidence maps produced by the base network becomes the prior for ThreshNet. With this, we can derive a Bayesian model for ThreshNet:

Given (X, Y) , where X is the set of input images and Y is the set of ground truths for the base segmentation network, the conditional probability distribution of the base network parameters θ is given by

$$p(\theta|X, Y) = \frac{p(\theta, X, Y)}{p(X, Y)} = \frac{p(Y|X, \theta)p(X, \theta)}{p(Y|X)p(X)} \quad (1)$$

$$\implies p(\theta|X, Y) = \frac{p(Y|X, \theta)p(\theta)}{p(Y|X)} \quad (2)$$

Let the parameters for ThreshNet be θ^* .

$$p(\theta^*|X, Y, \theta) = \frac{p(\theta^*, X, Y, \theta)}{p(X, Y, \theta)} = \frac{p(Y|X, \theta, \theta^*)p(X, \theta, \theta^*)}{p(\theta|X, Y)p(X, Y)} \quad (3)$$

$$= \frac{p(Y|X, \theta, \theta^*)p(X)p(\theta)p(\theta^*)p(Y|X)}{p(Y|X, \theta)p(\theta)p(Y|X)p(X)} \quad (4)$$

$$= \frac{p(Y|X, \theta, \theta^*)p(\theta^*)}{p(Y|X, \theta)} \quad (5)$$

$$\implies p(Y|X, \theta, \theta^*) = \frac{p(\theta^*|X, Y, \theta)p(Y|X, \theta)}{p(\theta^*)} \quad (6)$$

Here $p(Y|X, \theta)$ represents the output confidence map distribution of the base network which is the prior distribution for ThreshNet, and $p(Y|X, \theta, \theta^*)$ represents the output confidence map distribution of ThreshNet.

Given a test data point x^* , the prediction of the auxiliary model ThreshNet y^* is calculated by marginalizing the likelihood of the test input over the posterior through a posterior predictive distribution,

$$p(y^*|x^*, X, Y) = \int_{\theta^*} \int_{\theta} \underbrace{p(y^*|x^*, \theta, \theta^*)p(y^*|x, \theta)p(\theta^*|X, Y, \theta)}_{\text{cascading effect}} d\theta d\theta^* \quad (7)$$

From Eq. (7), we can note that the final refined output y^* is produced when ThreshNet (f^{θ^*}) is cascaded with the base segmentation network (f^{θ}).

$$y^* = f^{\theta^*}[f^{\theta}(x^*)] \quad (8)$$

3.2. Ground truth generation

In Sec. 1, we explained that converting confidence/probability maps into binary predictions can benefit from using region-specific thresholds rather than a fixed global threshold. Region-specific thresholds are not available during inference-time, so the goal of ThreshNet is to predict what the effect of these thresholds on the confidence maps would have been. During *training time* for ThreshNet, however, region-specific thresholds for each image can be computed. Part of the loss function is based on how well the output of ThreshNet matches the result of region-specific thresholding.

In order to compute this region-specific thresholding ground truth, we ensure that probability maps given as input to ThreshNet have been resized to 512×512 . For a patch size of $P \times P$, there are $N = (\frac{512}{P})^2$ number of patches. For each patch P_i of size $P \times P$ in an input probability map X , we calculate mIoU between that patch and corresponding ground truth binary segmentation by varying threshold values in the range $[0.05, 0.95]$, at intervals of 0.05. Let mIoU_array_{P_i} be the array of mIoUs corresponding to all of these candidate thresholds for the given patch P_i . Then, the best threshold for that patch is $\text{th}_{P_i}^* = \text{argmax}(\text{mIoU_array}_{P_i}) * 0.05$. Similarly, this is calculated for all patches P_i from $i = 1$ to N . Finally, the best set of thresholds th_P^* for patch size P are used to threshold the input probability map to get the region-specific thresholded map $Y_{\text{th}_P^*}$.

3.3. Framework

The overall pipeline of ThreshNet is illustrated in Fig. 3. **Training Stage.** Given an input probability map \mathbf{X} (output of a base segmentation model) resized to shape $512 \times 512 \times 1$, we use the residual encoder [21] with pyramid pooling [51] at the bottleneck to extract a global contextually-rich feature map of size $64 \times 64 \times 256$ ($\frac{1}{8}$ th decrease in resolution). This feature map is simultaneously given as input to the global and local decoder branches. The global branch decoder processes entire feature maps from the encoder to capture global inter-patch semantics. At each decoding step, the upsampled feature map from the previous decoder level is concatenated with self-attention-weighted [40] skip connection from the previous encoder level. This repeats over three decoding levels to finally produce an output $\hat{\mathbf{Y}}_G$ of shape $512 \times 512 \times 1$, as shown in Fig. 3. If the patch size is chosen to be P , a $P \times P$ patch at the beginning of the encoder becomes a $\frac{P}{8} \times \frac{P}{8}$ patch after pyramid pooling, with a $2 \times$ reduction in spatial resolution at every encoding step.

The local branch decoder parses each patch of the feature map independently to capture local intra-patch semantics. At each decoding step, a feature patch from the previous

decoder level is upsampled and concatenated with the corresponding self-attention-weighted [40] feature patch skip connection from the previous encoder level. This is repeated for all feature patches. The processed feature patches are spatially merged to get the original resolution at that decoder level. This repeats over three decoding levels to finally produce an output $\hat{\mathbf{Y}}_L$ of shape $512 \times 512 \times 1$, as shown in Fig. 3. The outputs are compared with the optimal region-specific thresholded map $\mathbf{Y}_{\text{th}_P^*}$ and the original ground truth binary segmentation \mathbf{Y} . For comparison with original ground truth map, we use the binary cross-entropy loss, and for comparison with region-specific-thresholded map, we use a combination of focal loss [33] and boundary loss which uses the Laplace Operator [17].

Inference Stage. During testing, the confidence/probability map generated by a base network is passed as input to the ThreshNet network trained with a patch size P . ThreshNet outputs an adjusted confidence map via the global branch and another adjusted confidence map via the local branch. These two confidence maps are averaged and then thresholded at 0.5 to get the final binary segmentation.

3.4. Network Architecture

Region-specific thresholds can be viewed as bias values between 0 and 1, and learning them as a regression task will work poorly as there is no spatial coherence between the 2D probability maps and 1D vector of threshold values. Hence, we design ThreshNet as a fully convolutional framework such that it can implicitly learn region-specific thresholds by exploiting global and local spatial information from input probability maps. The encoder captures global context. The two decoder branches pick up signals globally from entire feature maps, as well as locally from each patch of feature maps.

Encoder. We use a standard U-Net [43] encoder with ResNet-34 [21] backbone to extract features from input probability maps, as shown in Fig. 3. The spatial resolution decreases from 512 to 64 ($\frac{1}{8}$ th reduction), while the number of features increases from 32 to 256 at the end of four encoding levels. After the last encoding level pyramid pooling [51] with pooling sizes $[1, 2, 4, 8]$ is used at the bottleneck to capture global context. At the end of the pooling layer, the final resolution is $64 \times 64 \times 256$. For designing the encoder, we must also note that this model must be able to accommodate different patch sizes. With the final feature map resolution being 64×64 and a patch size of 16×16 , the patch size of the feature map at the bottleneck will be 2×2 , which is the lowest this model design can handle. There is a trade-off between the depth of the model and the patch size it can handle. From experiments on a small validation set that is used for hyperparameter tuning, we chose the final

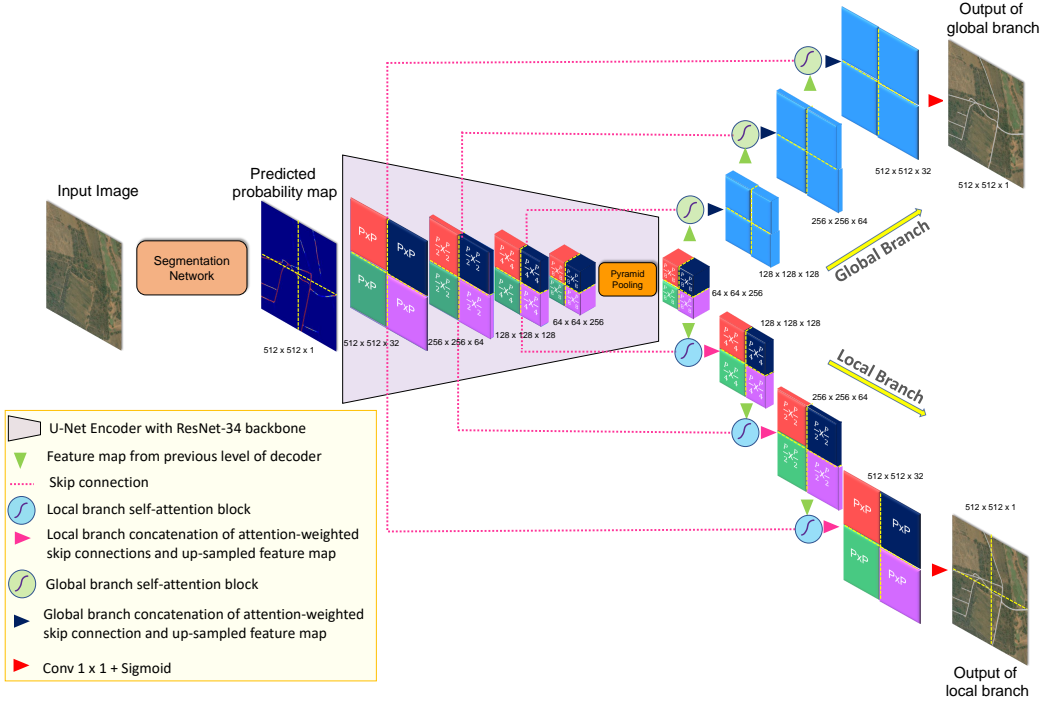


Figure 3. **Illustration of ThreshNet framework for $N=4$ patches (Patch Size $P = 256$)**. A confidence/probability map generated by a base model is passed as input to a U-Net [43] encoder with ResNet-34 [21] backbone. The encoder has 4 stages, which reduces the spatial resolution from 512 to 64 (i.e., $\frac{1}{8}^{th}$), thereby decreasing the patch size from P to $\frac{P}{8}$. Pyramid pooling [51] is used for building global context by aggregating features from four different scales. This rich context-aggregated feature map is then passed as input to two decoder branches – a *global* branch and a *local* branch. The global branch parses entire feature maps (similar to typical decoders) to capture inter-patch semantics. The local branch separately considers each feature patch independently to capture intra-patch semantics. This architecture can be used for any patch size from 256×256 to 16×16 .

resolution at the end of the bottleneck to be 64×64 .

Global Decoder Branch. This is a typical U-Net decoder with convolutional blocks, as shown in Fig. 3. We add a self-attention layer at each decoding level before concatenating skip connection from the previous encoder level with an upsampled feature map from the previous decoder layer. Self-attention [40] filters highlight salient features from spatial-information-rich skip connections and context-rich decoder (deeper) layers. This branch is used to extract global inter-patch interactions from the feature maps.

Local Decoder Branch. The design of this decoder is similar to that of the Global decoder. However, the core purpose of this branch is to capture local intra-patch semantics independently from each feature patch. The local branch self-attention block shown in Fig. 3 is magnified in Fig. 4. The feature map from decoder level i of size $p \times p \times D$ is broken down into $\frac{p}{2} \times \frac{p}{2} \times D$ sized patches. The skip connection from encoder level $i+1$ of size $2p \times 2p \times \frac{D}{2}$ is also broken down into $p \times p \times \frac{D}{2}$ sized patches. Each patch from

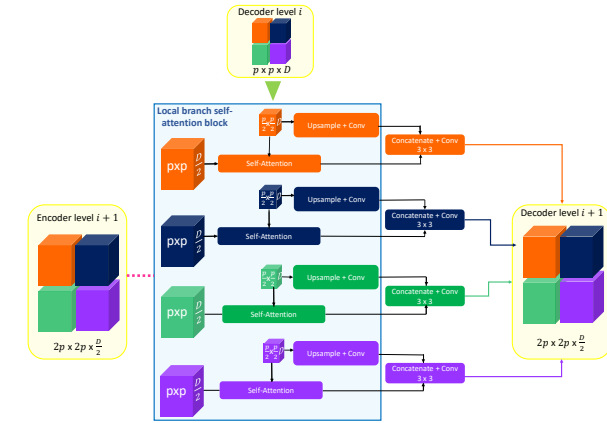


Figure 4. **Magnified local branch self-attention block for patch size $P = 4$** . The inputs to this block are the feature map from decoder level i and skip connection from encoder level $i+1$.

the decoder level i is upsampled and concatenated with the attention-weighted patch from the encoder level $i+1$. Finally, the processed patches are spatially merged to a shape

of $2p \times 2p \times \frac{D}{2}$, which is the output of decoder level $i + 1$. With this, each feature patch from a decoder level, along with the corresponding skip connection from the previous encoder level are processed separately, thereby capturing local semantics from each patch. The design of this branch allows the training to be performed simultaneously, as opposed to other patch aggregation methods [9, 46] that process local and global features as separate steps during training.

3.5. Loss Function

The region-specific loss L_{rs} is a combination of focal loss and boundary loss between global and local branch predictions \hat{Y}_G and \hat{Y}_L with region-specific-thresholded ground truth $Y_{th_P^*}$. The regularization loss L_{reg} , is a binary cross entropy loss for comparison of global and local branch predictions \hat{Y}_G and \hat{Y}_L with the original ground truth segmentation Y . L_{rs} focuses on refining pixels at a local level, while ignoring global structure. This will help the model learn patch-specific features. Focal loss will help the model concentrate on harder-to-segment pixels, while boundary loss helps in producing sharper boundary. L_{reg} provides a regularization effect by making the predictions more continuous and smoother by helping the model preserve the global structure. L_{rs} has two terms: L_{focal} and $L_{boundary}$.

$$L_{focal} = -(1 - c_t)^\gamma \log(c_t), \begin{cases} c_t = c, & Y_{th_P^*} = 1 \\ c_t = 1 - c, & \text{otherwise} \end{cases} \quad (9)$$

where $c \in [0, 1]$ is the model's estimated probability and $\gamma = 2$. To encourage better boundary refinement, we use a simple boundary loss as used in [44]. The Laplace operator (edge detector) is first used to get boundaries of predicted maps and ground truth maps. Cross-entropy loss is then used to encourage better boundary adherence. The Laplace operator is given by

$$\Delta f = \frac{\partial^2 f}{\partial x^2} + \frac{\partial^2 f}{\partial y^2} \quad (10)$$

Since the Laplace operator uses the gradient of the maps, it internally calls the convolution operation:

$$\tilde{\Delta f} = \text{abs}(\tanh(\text{conv}(f, K_{laplace})))$$

where $K_{laplace}$ is a 3×3 sobel filter.

$$L_{boundary} = -\Delta Y_{th_P^*} \log(\Delta \hat{Y}) - (1 - \Delta Y_{th_P^*}) \log(1 - \Delta \hat{Y}) \quad (11)$$

The total region-specific loss is given by:

$$L_{rs} = L_{focal} + L_{boundary} \quad (12)$$

The regularization loss L_{reg} is defined by:

$$L_{reg} = -\Delta Y \log(\Delta \hat{Y}) - (1 - \Delta Y) \log(1 - \Delta \hat{Y}) \quad (13)$$

The total loss for each branch is given by:

$$L = \alpha L_{rs} + (1 - \alpha) L_{reg} \quad \text{where } \alpha = 0.7 \quad (14)$$

4. Experiments

4.1. Datasets and Evaluation Criteria

We evaluate the performance of ThreshNet on two binary segmentation datasets - DeepGlobe [12] for geo-spatial segmentation and Kvasir-SEG [27] for histopathology segmentation. DeepGlobe is a large-scale road extraction dataset that contains 6226 labeled images. We divide this into 4980 training images, 996 validation images and 250 test images. Kvasir-SEG is a large-scale polyp segmentation dataset with 1000 labeled images. We divide this into 880 training images, 96 validation images and 24 test images. Further, we also evaluate the performance of ThreshNet on two more applications - we use the DUTS [44] dataset for Saliency detection. DUTS is a large-scale dataset that contains 10553 images for training and 5019 images for evaluation. We divide these 5019 images into 4015 validation images and 1004 test images. Similar to other state-of-the-art segmentation methods, we use mean Intersection over Union [42] (mIoU) and mean Boundary Accuracy (mBA) as the evaluation metrics [10]. mBA, also called boundary IoU, is a new measure proposed by [10] which has a weaker bias toward large objects than mIoU. It neither over-penalizes nor ignores errors in small objects. Given the ground truth mask G and predicted mask P , Boundary IoU first computes the set of the pixels that are within a distance d from each contour, and then computes IoU of these two sets.

$$\text{mBA}(G, P) = \frac{|(G_d \cap G) \cap (P_d \cap P)|}{|(G_d \cap G) \cup (P_d \cap P)|} \quad (15)$$

where G_d and P_d are sets of all pixels with distance d from the ground truth and prediction contours respectively. As mentioned [10], we use $d = 15$. We extract the contours by subtracting the morphologically eroded [26] maps from the original maps. We evaluate the performance of ThreshNet on Saliency detection [52] using mean absolute error (MAE), along with mIoU and mBA.

4.2. Implementation Details

Every dataset used in the paper is divided into training, validation and test sets as described in Sec. 4.1. The base model is trained on the training set, and validation data is

used for hyperparameter tuning. This validation data is used as training data for ThreshNet. A common test set is used to compare performances of the base model and ThreshNet. We do not use any validation data for training ThreshNet. It is trained until training loss converges. To make ThreshNet robust and to increase the amount of data available for training ThreshNet, we adopt some data augmentation techniques: Random rotation, horizontal and vertical flips. We use pre-trained base models (if available) to extract confidence maps, or train our base models with the specifications provided in their respective papers. ThreshNet is trained with the Adam [29] optimizer with an initial learning rate of $8e^{-4}$, batch size of 4 and for 300 epochs on a Nvidia 2080 Ti GPU. The learning rate is decreased until $5e^{-8}$ with a patience of 5 epochs. We use early stopping if training loss does not decrease for 10 epochs. Probability maps given as input to ThreshNet are of size $512 \times 512 \times 1$. Global and local branches are trained with the loss function as mentioned in Sec. 3.5. α value in the final loss function is set to 0.7, and the γ value for Focal loss is set to 2 as in [33].

4.3. Ablation Experiments

We perform ablation studies to show the efficacy of ThreshNet design and the choice of loss functions.

Choosing patch size (P). Fig. 5 presents the refinement

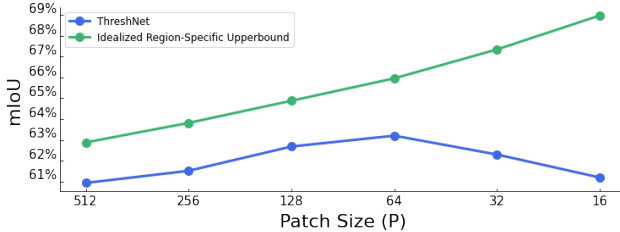


Figure 5. **ThreshNet vs. Optimal (idealized) choice of region-specific thresholding.** ThreshNet achieves near-ideal performance until $P = 64$, after which the performance drops due to lack of available local information that can be decoded.

quality, in terms of mIoU, achieved by ThreshNet on DeepGlobe [12] test set when trained with different values of P , where it is compared to the optimal choice of region-specific thresholding. The refinement quality of ThreshNet decreases after it reaches a maximum at a patch size of 64. This is due to lower amounts of signal in small patches and is also due to the decrease in the amount of local information in each feature patch available at the bottleneck for the local branch decoder to pick up. For $P = 32$ and $P = 16$, corresponding feature map patches at the bottleneck are of sizes 4×4 and 2×2 , which are too small to decode. For P values from 512 to 64, we can observe that ThreshNet is able to achieve near-ideal refinement quality with $\approx 2\%$ behind respective optimally chosen region-specific thresh-

olding upperbounds. A similar trend can be observed for all other datasets as well. In all our experiments, we choose $P = 64$ to get the maximum refinement quality achievable by ThreshNet.

Configuration	DeepGlobe [12]	
	mIoU (%)	mBA (%)
Base Network: D-LinkNet [54]	60.1	49.8
Ablation of decoder design		
Global branch only	60.5 \uparrow 0.4	52.3 \uparrow 2.5
Local branch only	62.3 \uparrow 2.2	56.1 \uparrow 6.3
Local + Global (ours)	63.2\uparrow3.1	56.6\uparrow6.8
Ablation of total loss function		
L_{reg} only	60.8 \uparrow 0.7	52.8 \uparrow 3.0
L_{rs} only	62.6 \uparrow 2.5	57.2 \uparrow 7.4
$L_{reg} + L_{rs}$ (ours)	63.2\uparrow3.1	56.6\uparrow6.8
Ablation of Region-specific loss L_{rs}		
Focal loss only	62.8 \uparrow 2.7	51.9 \uparrow 2.1
Boundary loss only	61.0 \uparrow 0.9	55.4 \uparrow 5.6
Focal + Boundary loss (ours)	63.2\uparrow3.1	56.6\uparrow6.8

Table 1. **Ablation study for ThreshNet ($P = 64$) design on DeepGlobe test set.** With the proposed Global + Local branches and loss function, ThreshNet achieves maximum refinement over the input base network.

ThreshNet Design. Table 1 shows an ablation study for the ThreshNet design. Using the $P = 64$ from the patch size ablation study from Fig. 5, we perform ablation experiments based on three design choices - decoder, total loss function and region-specific loss L_{rs} . For the choice of decoder, it can be observed that using only the global branch results in lowest mIoU and mBA. This shows the need for a local branch. Using only a local branch has better performance than using only a global branch. However, using both results in a performance boost. This shows that the global branch, which extracts inter-patch semantics, is also necessary for achieving better performance. Table 1 also shows the necessity of both L_{reg} and L_{rs} losses in the total loss function. L_{rs} captures local and global semantics from both branches. However, it can be seen that L_{reg} is also necessary as a regularization loss that helps in capturing global structure from the original ground truth. The ablation study for L_{rs} is also shown in the table. ThreshNet is a refinement module, which means only a few regions in input probability maps require refinement. This makes it important for the loss function to penalize hard-to-segment pixels that need more attention. This is where focal loss helps. Additionally, it can also be seen that boundary loss alone cannot achieve good refinement performance.

4.4. Performance Evaluation

ThreshNet can refine input probability maps by implicitly learning region-specific thresholds. In this section, we provide qualitative and quantitative results showcasing the performance of ThreshNet when paired with existing segmentation methods. We also show ThreshNet’s performance against other refinement methods. Further, we provide results for ThreshNet applied to the application of saliency detection.

Segmentation Refinement on DeepGlobe [12] & Kvasir-SEG [27].

DeepGlobe [12]		
Methods	mIoU (%)	mBA (%)
FCN-8s [37]	48.6	31.7
(+) ThreshNet	54.1\uparrow5.5	42.3\uparrow10.6
U-Net [43]	55.8	37.6
(+) ThreshNet	60.9\uparrow5.1	47.4\uparrow9.8
DeepLabV3+ [5]	59.2	47.6
(+) ThreshNet	61.9\uparrow2.7	55.9\uparrow8.3
PSPNet [51]	59.8	48.2
(+) ThreshNet	62.4\uparrow2.6	56.6\uparrow8.4
D-LinkNet [54]	60.1	49.8
(+) ThreshNet	63.2\uparrow3.1	56.6\uparrow6.8
Kvasir-SEG [27]		
Methods	mIoU (%)	mBA (%)
U-Net [43]	41.5	38.8
(+) ThreshNet	47.8\uparrow6.3	46.3\uparrow7.5
ResUnet [13]	46.8	45.7
(+) ThreshNet	52.9\uparrow6.1	52.5\uparrow6.8
ResUnet++ [28]	55.9	56.8
(+) ThreshNet	61.7\uparrow5.8	62.9\uparrow6.1

Table 2. **Quantitative results for ThreshNet (P = 64) on DeepGlobe and Kvasir-SEG test datasets.** This table shows performance of ThreshNet when paired with existing segmentation networks.

Table 2 quantitatively shows the performance of ThreshNet on DeepGlobe and Kvasir-SEG datasets when appended to existing segmentation networks. Our results show that ThreshNet consistently improves segmentation quality over existing segmentation networks. Fig. 6 and Fig. 7 show samples from DeepGlobe and Kvasir-SEG datasets that have been refined by ThreshNet. It can be clearly seen from highlighted yellow boxes that ThreshNet is able to guide low confidence false negative regions towards higher confidence scores, and high confidence false positive regions towards lower confidence scores, thereby achieving better segmentation and boundary quality. Tab. 2 shows that ThreshNet provides maximum improvement over base networks that have higher uncertainty in their predictions. As complexity of base networks increase towards state-

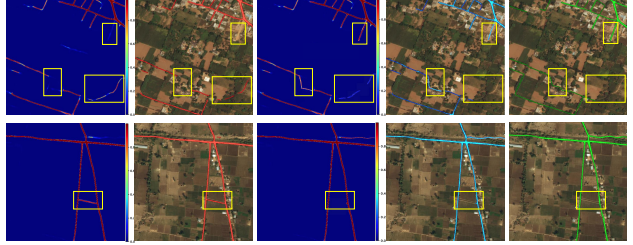


Figure 6. **Qualitative results produced by ThreshNet (P = 64) on samples from DeepGlobe test dataset.** Left to right: Probability map from base network D-LinkNet, Thresholded (0.5) prediction from D-LinkNet, Refined probability map from ThreshNet, Thresholded (0.5) prediction from ThreshNet, Ground Truth. Yellow boxes denote regions of refinement.

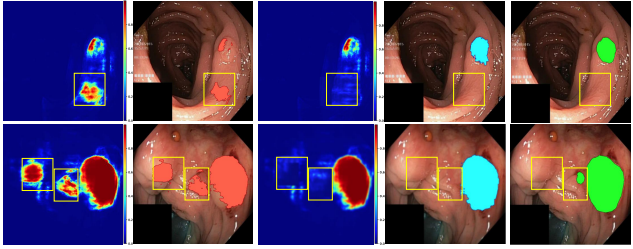


Figure 7. **Qualitative results produced by ThreshNet (P = 64) on samples from Kvasir-SEG test dataset.** Left to right: Probability map from base network ResUnet++, Thresholded (0.5) prediction from ResUnet++, Refined probability map from ThreshNet, Thresholded (0.5) prediction from ThreshNet, Ground Truth. Yellow boxes denote regions of refinement.

of-the-art, the amount of refinement decreases. Although existing base networks are able to achieve state-of-the-art results, it can be seen from Fig. 6 and Fig. 7 that there are hard samples on which they fail. These samples are picked up by ThreshNet and refined. Overall, ThreshNet is able to achieve 5.8% and 3.1% improvement in mIoU over state-of-the-art models for Kvasir-SEG and DeepGlobe datasets respectively.

Saliency detection on DUTS [44]. We extend ThreshNet to Saliency detection. It can be seen from Tab. 3 and Fig. 8 that ThreshNet is able to achieve better segmentation and boundary quality when paired with existing saliency detection methods. Overall, ThreshNet is able to achieve 3.8% improvement over one of the state-of-the-art methods for saliency detection.

Comparison with DenseCRF [5]. In this section, we compare the performance of ThreshNet with DenseCRF [5], which is a popular method for post-processing segmentation maps.

We performed grid search on DeepGlobe, Kvasir-SEG and DUTS datasets to find the respective hyperparameters,

DUTS [44]			
Methods	mIoU (%)	mBA (%)	MAE
RFCN [45]	52.8	40.7	0.0897
(+) ThreshNet	57.1\uparrow4.3	48.5\uparrow7.8	0.0807
PFAN [52]	66.1	51.2	0.0452
(+) ThreshNet	69.9\uparrow3.8	58.6\uparrow7.4	0.0386

Table 3. Performance of ThreshNet refinement on DUTS Saliency detection test dataset.

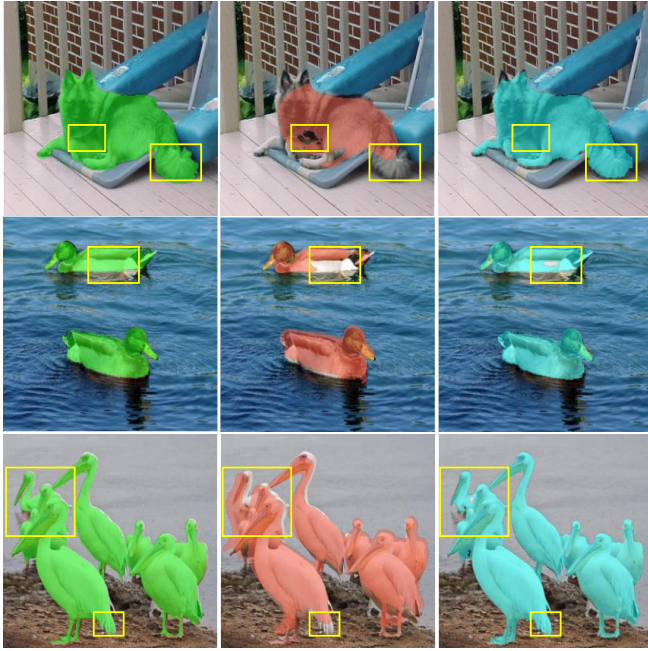


Figure 8. Qualitative results produced by ThreshNet ($P = 64$) on samples from DUTS Saliency detection test dataset. Left to right: Ground Truth, Thresholded (0.5) prediction from PFANet [52], Refined map by ThreshNet. Yellow boxes denote regions of refinement.

DUTS		
Methods	mIoU (%)	mBA (%)
RFCN [45]	52.8	40.7
(+) DenseCRF	54.6 \uparrow 1.8	42.2 \uparrow 1.5
(+) ThreshNet	57.1\uparrow4.3	48.5\uparrow7.8
PFAN [52]	66.1	51.2
(+) DenseCRF	67.0 \uparrow 0.9	52.4 \uparrow 1.2
(+) ThreshNet	69.9\uparrow3.8	58.6\uparrow7.4

Table 4. Quantitative results comparing ThreshNet ($P=64$) with DenseCRF on DUTS saliency detection dataset.

as suggested in the original paper [5]. Tab. 4, Tab. 5 and Tab. 6 tabulate quantitative results of performance comparison. Fig. 9 shows the qualitative comparison between ThreshNet and DenseCRF refinement. It can be observed

Kvasir-SEG		
Methods	mIoU (%)	mBA (%)
U-Net [43]	41.5	38.8
(+) DenseCRF	43.2 \uparrow 1.7	41.6 \uparrow 2.8
(+) ThreshNet	47.8\uparrow6.3	46.3\uparrow7.5
ResUnet [13]	46.8	45.7
(+) DenseCRF	48.3 \uparrow 1.5	47.1 \uparrow 1.4
(+) ThreshNet	52.9\uparrow6.1	52.5\uparrow6.8
ResUnet++ [28]	55.9	56.8
(+) DenseCRF	56.8 \uparrow 0.9	58.2 \uparrow 1.4
(+) ThreshNet	61.7\uparrow5.8	62.9\uparrow6.1

Table 5. Quantitative results comparing ThreshNet ($P=64$) with DenseCRF on Kvasir-SEG dataset.

DeepGlobe [12]		
Methods	mIoU (%)	mBA (%)
FCN-8s [37]	48.6	31.7
(+) DenseCRF	50.9 \uparrow 2.3	34.9 \uparrow 3.2
(+) ThreshNet	54.1\uparrow5.5	42.3\uparrow10.6
U-Net [43]	55.8	37.6
(+) DenseCRF	57.6 \uparrow 1.8	40.5 \uparrow 2.9
(+) ThreshNet	60.9\uparrow5.1	47.4\uparrow9.8
DeepLabV3+ [5]	59.2	47.6
(+) DenseCRF	59.9 \uparrow 0.7	49.3 \uparrow 1.7
(+) ThreshNet	61.9\uparrow2.7	55.9\uparrow8.3
PSPNet [51]	59.8	48.2
(+) DenseCRF	60.3 \uparrow 0.5	49.7 \uparrow 1.5
(+) ThreshNet	62.4\uparrow2.6	56.6\uparrow8.4
D-LinkNet [54]	60.1	49.8
(+) DenseCRF	60.8 \uparrow 0.7	51.4 \uparrow 1.6
(+) ThreshNet	63.2\uparrow3.1	56.6\uparrow6.8

Table 6. Quantitative results comparing ThreshNet ($P=64$) with DenseCRF on DeepGlobe dataset.

that DenseCRF is unable to remove false positives and false negatives from the segmentation maps. This is because, DenseCRF is an unsupervised method that does not capture global semantics between pixels regions. It is only able to achieve smoothing along the boundary, which is the cause for a small improvement in mIoU and mBA. We also observed that applying DenseCRF to ThreshNet does not provide any significant improvement in performance across all datasets.

Comparison with CascadePSP [11]. We train a U-Net model on DeepGlobe dataset, and refine the predictions with CRF [5], Cascade-PSP [11] and ThreshNet refinement modules as shown in Tab. 7. ThreshNet outperforms a 3-level cascaded refinement module by 1.1%, and unsupervised CRF refinement by 3.3%. It can also be seen that ThreshNet has the best memory-accuracy trade-off with

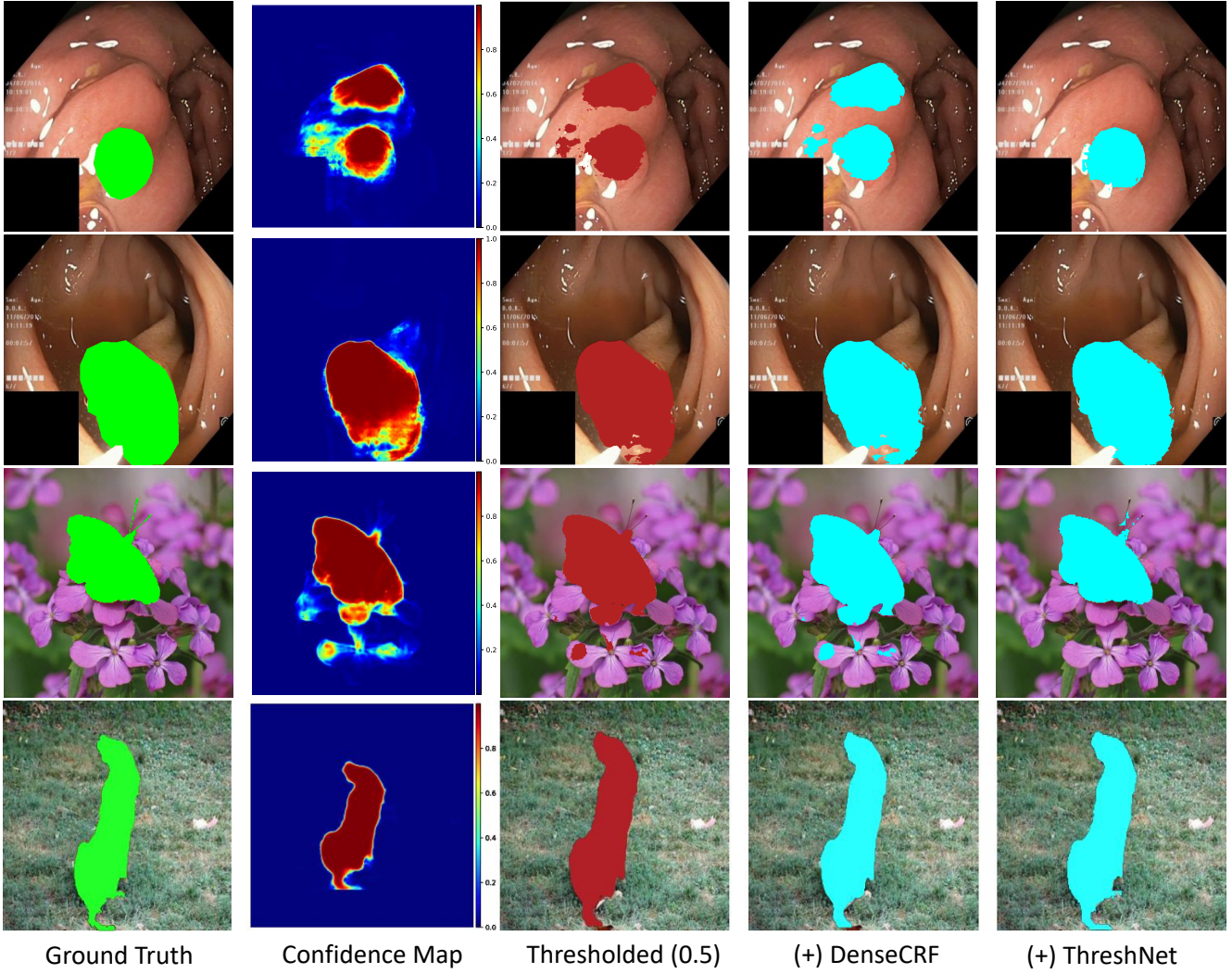


Figure 9. Qualitative results comparing performance of ThreshNet (P=64) with DenseCRF on samples from Kvasir-SEG (first 2 rows) and DUTS saliency detection (last 2 rows) test datasets. Left to Right: Ground Truth, Probability map from base network, Thresholded (0.5) prediction from base network, DenseCRF refined map, ThreshNet refined map.

DeepGlobe [12]		
Methods	mIoU (%)	memory usage
U-Net [43]	55.8	3.16 GB
(+) CascadePSP [11] 3-level	59.8 \uparrow 4.0	
U-Net [43]	55.8	1.03 GB
(+) ThreshNet	60.9\uparrow5.1	

Table 7. Comparison of CascadePSP with ThreshNet on DeepGlobe test set.

only 1.03 GB GPU memory utilization as compared to 3.16 GB used by Cascade PSP.

More qualitative results. Fig. 10, Fig. 11 and Fig. 12 show qualitative results for ThreshNet (P=64) refinement

when applied to DeepGlobe, DUTS saliency detection and Kvasir-SEG datasets respectively. Yellow boxes mark the regions of refinement. It can be observed that ThreshNet is able to achieve significant visual improvement compared to the corresponding segmentation maps from state-of-the-art base networks with fixed (0.5) thresholding.

5. Conclusion

We propose ThreshNet refinement framework inspired by region-specific-thresholding for improving quality of segmentation maps generated by an existing base network. Even when the base network is state-of-the-art, ThreshNet is able to significantly improve mIoU and mBA. ThreshNet can also be extended to saliency detection, and any other applications that use

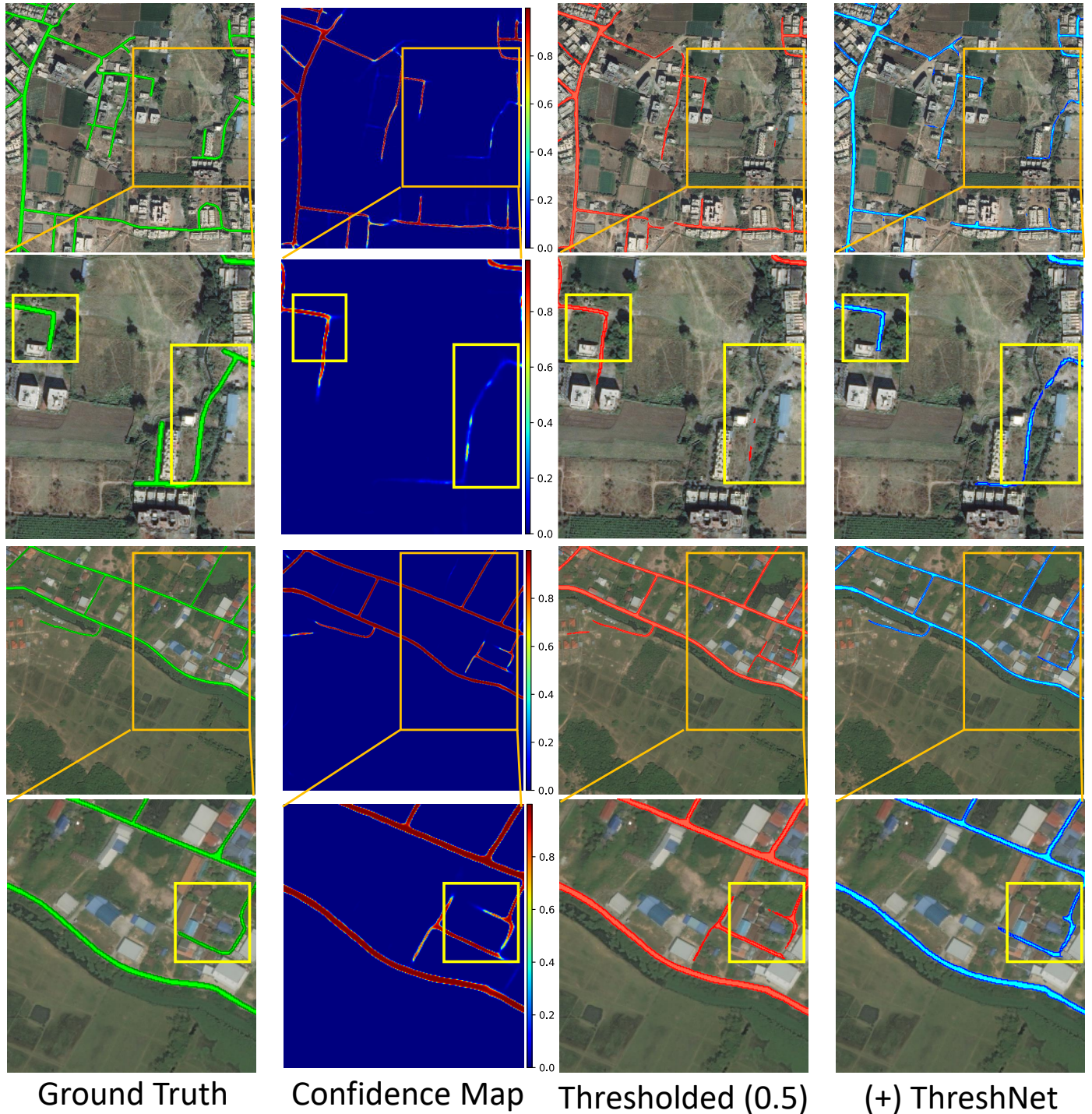


Figure 10. **Qualitative results produced by ThreshNet (P=64) on samples from DeepGlobe test dataset.** Left to Right: Ground Truth, Probability map from base network D-LinkNet, Thresholded (0.5) prediction from D-LinkNet, Refined thresholded (0.5) prediction from ThreshNet.

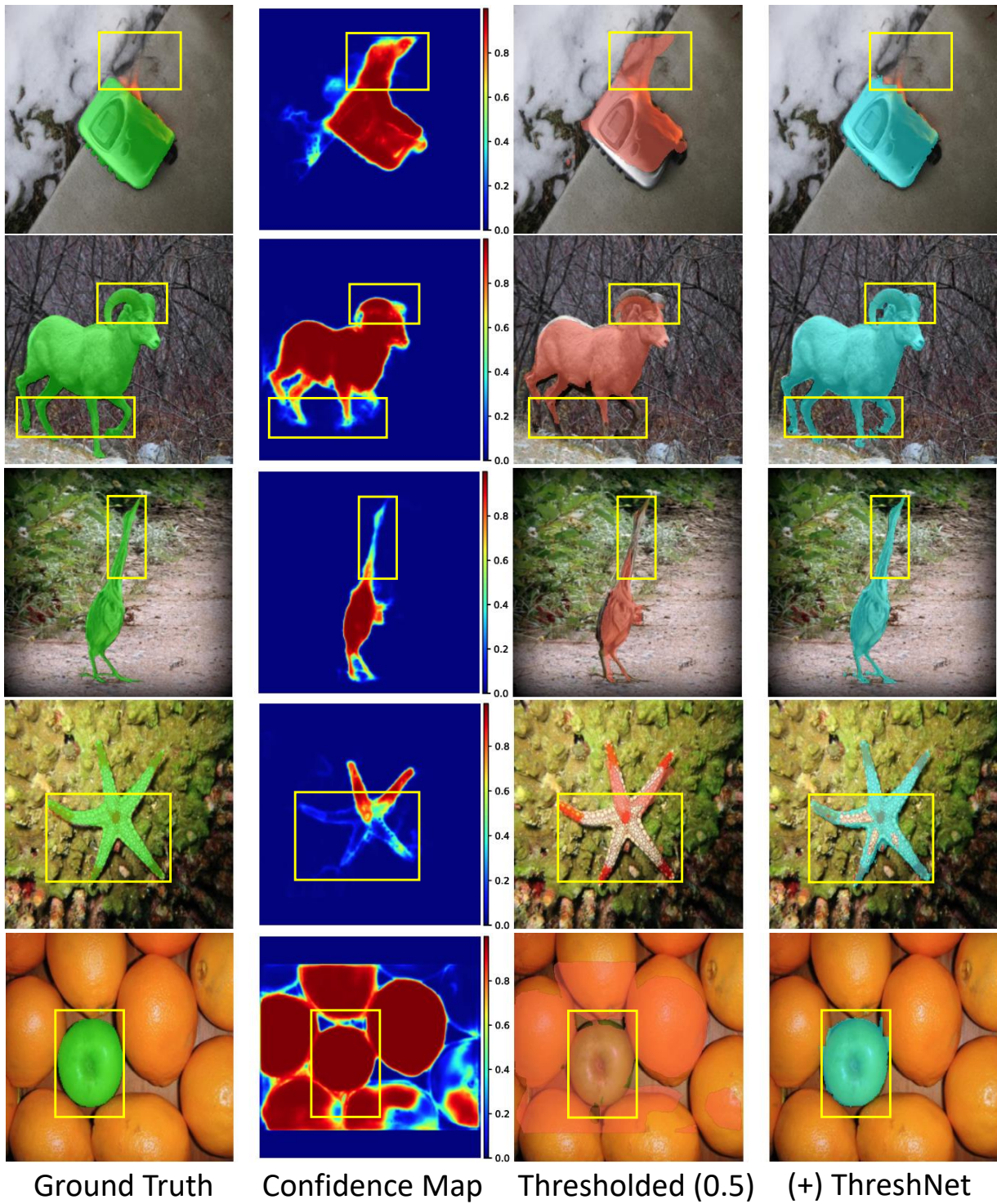


Figure 11. **Qualitative results produced by ThreshNet (P=64) on samples from DUTS saliency detection test dataset.** Left to Right: Ground Truth, Probability map from base network PFAN, Thresholded (0.5) prediction from PFAN, Refined thresholded (0.5) prediction from ThreshNet.

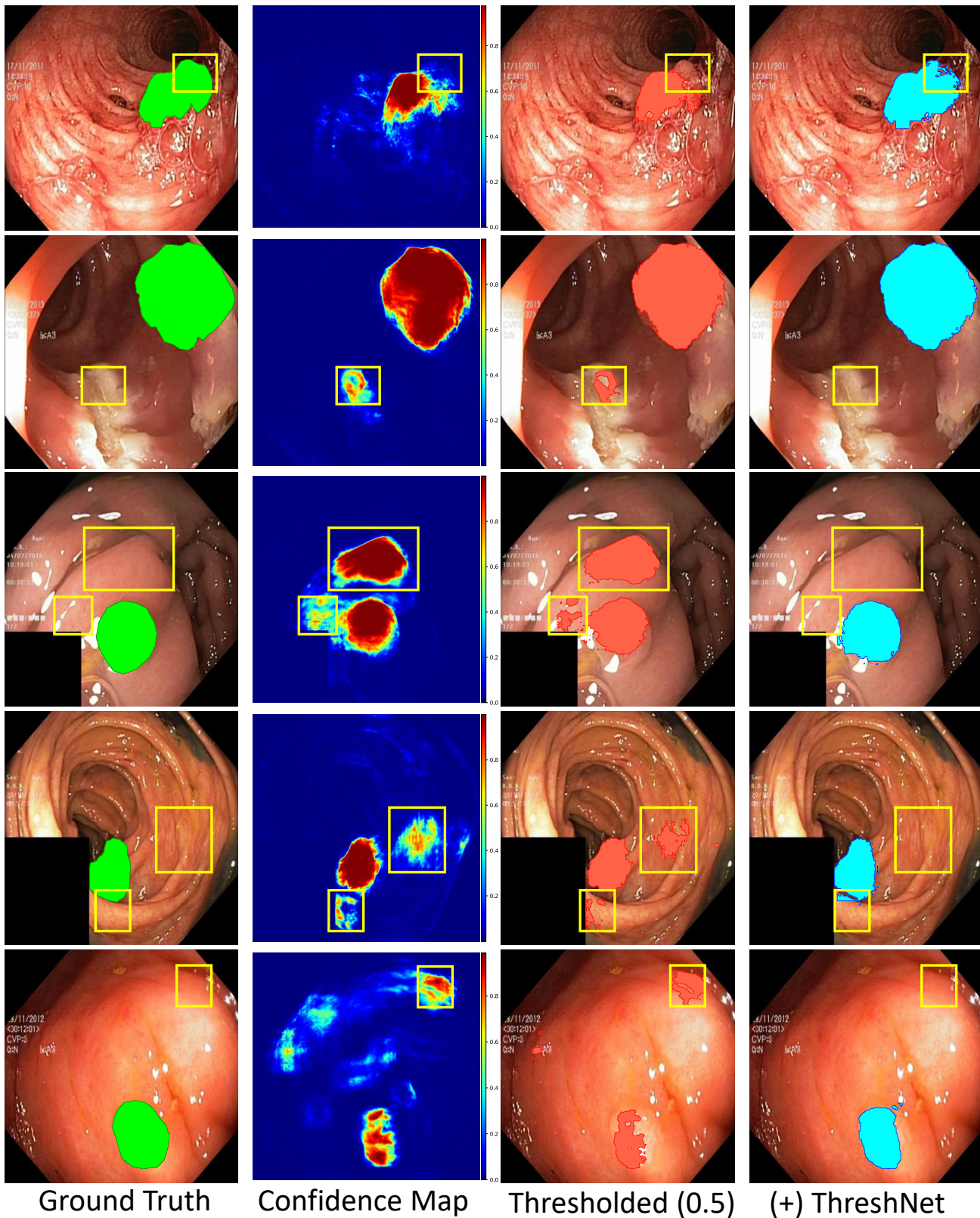


Figure 12. **Qualitative results produced by ThreshNet ($P=64$) on samples from Kvasir-SEG test dataset.** Left to Right: Ground Truth, Probability map from base network ResNet++, Thresholded (0.5) prediction from ResNet++, Refined thresholded (0.5) prediction from ThreshNet.

binary annotations. With our experiments, we show that ThreshNet improves segmentation quality by 3-5% when paired with any existing base networks. However, the quality of segmentation maps produced by ThreshNet is dependent on how good the base network is.

References

[1] Marjan Alirezaie, Martin Längkvist, Michael Sioutis, and Amy Loutfi. Semantic referee: A neural-symbolic framework for enhancing geospatial semantic segmentation. *Semantic Web*, 10(5):863–880, 2019. [2](#)

[2] Vijay Badrinarayanan, Alex Kendall, and Roberto Cipolla. Segnet: A deep convolutional encoder-decoder architecture for image segmentation. *IEEE transactions on pattern analysis and machine intelligence*, 39(12):2481–2495, 2017. [2](#)

[3] Derek Bradley and Gerhard Roth. Adaptive thresholding using the integral image. *Journal of graphics tools*, 12(2):13–21, 2007. [3](#)

[4] Liang-Chieh Chen, George Papandreou, Iasonas Kokkinos, Kevin Murphy, and Alan L Yuille. Semantic image segmentation with deep convolutional nets and fully connected crfs. *arXiv preprint arXiv:1412.7062*, 2014. [3](#)

[5] Liang-Chieh Chen, George Papandreou, Iasonas Kokkinos, Kevin Murphy, and Alan L Yuille. Deeplab: Semantic image segmentation with deep convolutional nets, atrous convolution, and fully connected crfs. *IEEE transactions on pattern analysis and machine intelligence*, 40(4):834–848, 2017. [2](#), [3](#), [8](#), [9](#)

[6] Liang-Chieh Chen, George Papandreou, Florian Schroff, and Hartwig Adam. Rethinking atrous convolution for semantic image segmentation. *arXiv preprint arXiv:1706.05587*, 2017. [1](#)

[7] Liang-Chieh Chen, Yi Yang, Jiang Wang, Wei Xu, and Alan L Yuille. Attention to scale: Scale-aware semantic image segmentation. In *Proceedings of the IEEE conference on computer vision and pattern recognition*, pages 3640–3649, 2016. [2](#), [3](#)

[8] Liang-Chieh Chen, Yukun Zhu, George Papandreou, Florian Schroff, and Hartwig Adam. Encoder-decoder with atrous separable convolution for semantic image segmentation. In *Proceedings of the European conference on computer vision (ECCV)*, pages 801–818, 2018. [2](#)

[9] Wuyang Chen, Ziyu Jiang, Zhangyang Wang, Kexin Cui, and Xiaoning Qian. Collaborative global-local networks for memory-efficient segmentation of ultra-high resolution images. In *Proceedings of the IEEE/CVF Conference on Computer Vision and Pattern Recognition*, pages 8924–8933, 2019. [3](#), [6](#)

[10] Bowen Cheng, Ross Girshick, Piotr Dollár, Alexander C Berg, and Alexander Kirillov. Boundary iou: Improving object-centric image segmentation evaluation. In *Proceedings of the IEEE/CVF Conference on Computer Vision and Pattern Recognition*, pages 15334–15342, 2021. [2](#), [6](#)

[11] Ho Kei Cheng, Jihoon Chung, Yu-Wing Tai, and Chi-Keung Tang. Cascadepsp: Toward class-agnostic and very high-resolution segmentation via global and local refinement. In *Proceedings of the IEEE/CVF Conference on Computer Vision and Pattern Recognition*, pages 8890–8899, 2020. [2](#), [3](#), [9](#), [10](#)

[12] Ilke Demir, Krzysztof Koperski, David Lindenbaum, Guan Pang, Jing Huang, Saikat Basu, Forest Hughes, Devis Tuia, and Ramesh Raskar. Deepglobe 2018: A challenge to parse the earth through satellite images. In *Proceedings of the IEEE Conference on Computer Vision and Pattern Recognition Workshops*, pages 172–181, 2018. [1](#), [2](#), [6](#), [7](#), [8](#), [9](#), [10](#)

[13] Foivos I Diakogiannis, François Waldner, Peter Caccetta, and Chen Wu. Resunet-a: A deep learning framework for semantic segmentation of remotely sensed data. *ISPRS Journal of Photogrammetry and Remote Sensing*, 162:94–114, 2020. [8](#), [9](#)

[14] Philipe Ambrozio Dias and Henry Medeiros. Semantic segmentation refinement by monte carlo region growing of high confidence detections. In *Asian Conference on Computer Vision*, pages 131–146. Springer, 2018. [3](#)

[15] Philipe A Dias and Henry Medeiros. Probabilistic semantic segmentation refinement by monte carlo region growing. *arXiv preprint arXiv:2005.05856*, 2020. [3](#)

[16] Clement Farabet, Camille Couprie, Laurent Najman, and Yann LeCun. Learning hierarchical features for scene labeling. *IEEE transactions on pattern analysis and machine intelligence*, 35(8):1915–1929, 2012. [2](#)

[17] David Gilbarg, Neil S Trudinger, David Gilbarg, and NS Trudinger. *Elliptic partial differential equations of second order*, volume 224. Springer, 1977. [4](#)

[18] Stas Goferman, Lihi Zelnik-Manor, and Ayallet Tal. Context-aware saliency detection. *IEEE transactions on pattern analysis and machine intelligence*, 34(10):1915–1926, 2011. [2](#)

[19] Bharath Hariharan, Pablo Arbeláez, Ross Girshick, and Jitendra Malik. Hypercolumns for object segmentation and fine-grained localization. In *Proceedings of the IEEE conference on computer vision and pattern recognition*, pages 447–456, 2015. [3](#)

[20] Kaiming He, Xiangyu Zhang, Shaoqing Ren, and Jian Sun. Spatial pyramid pooling in deep convolutional networks for visual recognition. *IEEE transactions on pattern analysis and machine intelligence*, 37(9):1904–1916, 2015. [1](#), [2](#)

[21] Kaiming He, Xiangyu Zhang, Shaoqing Ren, and Jian Sun. Deep residual learning for image recognition. In *Proceedings of the IEEE conference on computer vision and pattern recognition*, pages 770–778, 2016. [4](#), [5](#)

[22] Xuming He, Richard S Zemel, and Miguel A Carreira-Perpinán. Multiscale conditional random fields for image labeling. In *Proceedings of the 2004 IEEE Computer Society Conference on Computer Vision and Pattern Recognition, 2004. CVPR 2004.*, volume 2, pages II–II. IEEE, 2004. [2](#)

[23] Xiaodi Hou and Liqing Zhang. Saliency detection: A spectral residual approach. In *2007 IEEE Conference on computer vision and pattern recognition*, pages 1–8. Ieee, 2007. [2](#)

[24] Gao Huang, Zhuang Liu, Laurens Van Der Maaten, and Kilian Q Weinberger. Densely connected convolutional networks. In *Proceedings of the IEEE conference on computer vision and pattern recognition*, pages 4700–4708, 2017. [1](#)

[25] Lang Huang, Yuhui Yuan, Jianyuan Guo, Chao Zhang, Xilin Chen, and Jingdong Wang. Interlaced sparse self-attention for semantic segmentation. *arXiv preprint arXiv:1907.12273*, 2019. 3

[26] Paul T. Jackway and Mohamed Deriche. Scale-space properties of the multiscale morphological dilation-erosion. *IEEE transactions on pattern analysis and machine intelligence*, 18(1):38–51, 1996. 6

[27] Debesh Jha, Pia H Smedsrød, Michael A Riegler, Pål Halvorsen, Thomas de Lange, Dag Johansen, and Håvard D Johansen. Kvasir-seg: A segmented polyp dataset. In *International Conference on Multimedia Modeling*, pages 451–462. Springer, 2020. 1, 2, 6, 8

[28] Debesh Jha, Pia H Smedsrød, Michael A Riegler, Dag Johansen, Thomas De Lange, Pål Halvorsen, and Håvard D Johansen. Resunet++: An advanced architecture for medical image segmentation. In *2019 IEEE International Symposium on Multimedia (ISM)*, pages 225–2255. IEEE, 2019. 1, 2, 3, 8, 9

[29] Diederik P Kingma and Jimmy Ba. Adam: A method for stochastic optimization. *arXiv preprint arXiv:1412.6980*, 2014. 7

[30] Boyi Li, Kilian Q Weinberger, Serge Belongie, Vladlen Koltun, and René Ranftl. Language-driven semantic segmentation. *arXiv preprint arXiv:2201.03546*, 2022. 1

[31] Hanchao Li, Pengfei Xiong, Jie An, and Lingxue Wang. Pyramid attention network for semantic segmentation. *arXiv preprint arXiv:1805.10180*, 2018. 2

[32] Xiang Li, Tianhan Wei, Yau Pun Chen, Yu-Wing Tai, and Chi-Keung Tang. Fss-1000: A 1000-class dataset for few-shot segmentation. In *Proceedings of the IEEE/CVF conference on computer vision and pattern recognition*, pages 2869–2878, 2020. 1, 2, 3

[33] Tsung-Yi Lin, Priya Goyal, Ross Girshick, Kaiming He, and Piotr Dollár. Focal loss for dense object detection. In *Proceedings of the IEEE international conference on computer vision*, pages 2980–2988, 2017. 4, 7

[34] Chenxi Liu, Liang-Chieh Chen, Florian Schroff, Hartwig Adam, Wei Hua, Alan L Yuille, and Li Fei-Fei. Auto-deeplab: Hierarchical neural architecture search for semantic image segmentation. In *Proceedings of the IEEE/CVF conference on computer vision and pattern recognition*, pages 82–92, 2019. 2

[35] Shu Liu, Lu Qi, Haifang Qin, Jianping Shi, and Jiaya Jia. Path aggregation network for instance segmentation. In *Proceedings of the IEEE conference on computer vision and pattern recognition*, pages 8759–8768, 2018. 2

[36] Wei Liu, Andrew Rabinovich, and Alexander C Berg. Parsenet: Looking wider to see better. *arXiv preprint arXiv:1506.04579*, 2015. 2

[37] Jonathan Long, Evan Shelhamer, and Trevor Darrell. Fully convolutional networks for semantic segmentation. In *Proceedings of the IEEE conference on computer vision and pattern recognition*, pages 3431–3440, 2015. 1, 2, 8, 9

[38] Savinay Nagendra, Daniel Kifer, Benjamin Mirus, Te Pei, Kathryn Lawson, Srikanth Banagere Manjunatha, Weixin Li, Hien Nguyen, Tong Qiu, Sarah Tran, et al. Constructing a large-scale landslide database across heterogeneous environments using task-specific model updates. *IEEE Journal of Selected Topics in Applied Earth Observations and Remote Sensing*, 15:4349–4370, 2022. 1, 2, 3

[39] Hyeonwoo Noh, Seunghoon Hong, and Bohyung Han. Learning deconvolution network for semantic segmentation. In *Proceedings of the IEEE international conference on computer vision*, pages 1520–1528, 2015. 2

[40] Ozan Oktay, Jo Schlemper, Loic Le Folgoc, Matthew Lee, Mattias Heinrich, Kazunari Misawa, Kensaku Mori, Steven McDonagh, Nils Y Hammerla, Bernhard Kainz, et al. Attention u-net: Learning where to look for the pancreas. *arXiv preprint arXiv:1804.03999*, 2018. 3, 4, 5

[41] Dzung L Pham, Chenyang Xu, and Jerry L Prince. A survey of current methods in medical image segmentation. *Annual review of biomedical engineering*, 2(3):315–337, 2000. 2

[42] Hamid Rezatofighi, Nathan Tsoi, JunYoung Gwak, Amir Sadeghian, Ian Reid, and Silvio Savarese. Generalized intersection over union: A metric and a loss for bounding box regression. In *Proceedings of the IEEE/CVF conference on computer vision and pattern recognition*, pages 658–666, 2019. 2, 6

[43] Olaf Ronneberger, Philipp Fischer, and Thomas Brox. U-net: Convolutional networks for biomedical image segmentation. In *International Conference on Medical image computing and computer-assisted intervention*, pages 234–241. Springer, 2015. 1, 2, 4, 5, 8, 9, 10

[44] Lijun Wang, Huchuan Lu, Yifan Wang, Mengyang Feng, Dong Wang, Baocai Yin, and Xiang Ruan. Learning to detect salient objects with image-level supervision. In *Proceedings of the IEEE conference on computer vision and pattern recognition*, pages 136–145, 2017. 1, 2, 6, 8, 9

[45] Linzhao Wang, Lijun Wang, Huchuan Lu, Pingping Zhang, and Xiang Ruan. Saliency detection with recurrent fully convolutional networks. In *European conference on computer vision*, pages 825–841. Springer, 2016. 9

[46] Tong Wu, Zhenzhen Lei, Bingqian Lin, Cuihua Li, Yanyun Qu, and Yuan Xie. Patch proposal network for fast semantic segmentation of high-resolution images. In *Proceedings of the AAAI Conference on Artificial Intelligence*, pages 12402–12409, 2020. 6

[47] Fangting Xia, Peng Wang, Liang-Chieh Chen, and Alan L Yuille. Zoom better to see clearer: Human and object parsing with hierarchical auto-zoom net. In *European Conference on Computer Vision*, pages 648–663. Springer, 2016. 3

[48] Linwei Ye, Mrigank Rochan, Zhi Liu, and Yang Wang. Cross-modal self-attention network for referring image segmentation. In *Proceedings of the IEEE/CVF conference on computer vision and pattern recognition*, pages 10502–10511, 2019. 3

[49] Fisher Yu and Vladlen Koltun. Multi-scale context aggregation by dilated convolutions. *arXiv preprint arXiv:1511.07122*, 2015. 2

[50] Yuhui Yuan, Jingyi Xie, Xilin Chen, and Jingdong Wang. Segfix: Model-agnostic boundary refinement for segmentation. In *European Conference on Computer Vision*, pages 489–506. Springer, 2020. 3

- [51] Hengshuang Zhao, Jianping Shi, Xiaojuan Qi, Xiaogang Wang, and Jiaya Jia. Pyramid scene parsing network. In *Proceedings of the IEEE conference on computer vision and pattern recognition*, pages 2881–2890, 2017. [4](#), [5](#), [8](#), [9](#)
- [52] Ting Zhao and Xiangqian Wu. Pyramid feature attention network for saliency detection. In *Proceedings of the IEEE/CVF conference on computer vision and pattern recognition*, pages 3085–3094, 2019. [1](#), [2](#), [3](#), [6](#), [9](#)
- [53] Zhuo Zheng, Yanfei Zhong, Junjue Wang, and Ailong Ma. Foreground-aware relation network for geospatial object segmentation in high spatial resolution remote sensing imagery. In *Proceedings of the IEEE/CVF conference on computer vision and pattern recognition*, pages 4096–4105, 2020. [2](#)
- [54] Lichen Zhou, Chuang Zhang, and Ming Wu. D-linknet: Linknet with pretrained encoder and dilated convolution for high resolution satellite imagery road extraction. In *Proceedings of the IEEE Conference on Computer Vision and Pattern Recognition Workshops*, pages 182–186, 2018. [1](#), [2](#), [3](#), [7](#), [8](#), [9](#)
- [55] Zongwei Zhou, Md Mahfuzur Rahman Siddiquee, Nima Tajbakhsh, and Jianming Liang. Unet++: A nested u-net architecture for medical image segmentation. In *Deep learning in medical image analysis and multimodal learning for clinical decision support*, pages 3–11. Springer, 2018. [2](#)
- [56] Zhen Zhou, Yan Zhou, Dongli Wang, Jinzhen Mu, and Haibin Zhou. Self-attention feature fusion network for semantic segmentation. *Neurocomputing*, 453:50–59, 2021. [3](#)